NEUROSCIENCE

Altered D-glucose in brain parenchyma and cerebrospinal fluid of early Alzheimer's disease detected by dynamic glucose-enhanced MRI

Jianpan Huang[1], Peter C. M. van Zijl[2,3], Xiongqi Han[1], Celia M. Dong[4], Gerald W. Y. Cheng[5], Kai-Hei Tse[5], Linda Knutsson[2,6], Lin Chen[2,3], Joseph H. C. Lai[1], Ed X. Wu[4], Jiadi Xu[2,3]*, Kannie W. Y. Chan[1,2,7]*

Altered cerebral glucose uptake is one of the hallmarks of Alzheimer's disease (AD). A dynamic glucose-enhanced (DGE) magnetic resonance imaging (MRI) approach was developed to simultaneously monitor D-glucose uptake and clearance in both brain parenchyma and cerebrospinal fluid (CSF). We observed substantially higher uptake in parenchyma of young (6 months) transgenic AD mice compared to age-matched wild-type (WT) mice. Notably lower uptakes were observed in parenchyma and CSF of old (16 months) AD mice. Both young and old AD mice had an obviously slower CSF clearance than age-matched WT mice. This resembles recent reports of the hampered CSF clearance that leads to protein accumulation in the brain. These findings suggest that DGE MRI can identify altered glucose uptake and clearance in young AD mice upon the emergence of amyloid plaques. DGE MRI of brain parenchyma and CSF has potential for early AD stratification, especially at 3T clinical field strength MRI.

INTRODUCTION

Alzheimer's disease (AD) is the most common form of dementia, accounting for 60 to 70% of this disease. It affects the patients' daily life in many ways, including impairments in memory, speaking, problem solving, and other basic life skills (*1*). Early AD stratification remains challenging because changes in current biomarkers often overlap with normal aging. Neuropathology of AD includes the overexpression of amyloid precursor protein (APP) that results in the deposition of β amyloid (Aβ) plaques and tau neurofibrillary tangles, thus leading to structural and functional brain abnormalities in AD (*1*). Recent findings suggested that a reduction in cerebrospinal fluid (CSF) transport is associated with elevated brain Aβ, especially in young AD mice without visible Aβ plaques (*2*). Moreover, a change in cerebral glucose uptake is one of the hallmarks of AD (*3*). Glucose hypermetabolism or hypometabolism in brain has been found in some AD mouse models in different stages of AD (*4*–*7*). Luo *et al.* and Poisnel *et al.* (*5*, *6*) both observed a higher glucose utilization in brains of young APP mice but a lower glucose utilization in aged APP mice compared to the age-matched wild-type (WT) mice. Many AD drugs are being developed using transgenic mouse models of amyloidosis-expressing mutant forms of human APP and presenilin-1 (PS1) (*8*), which is well known to reproduce some of the neuropathology observed in humans. Thus, glucose utilization and CSF clearance serve as important imaging biomarkers for early AD stratification.

Currently, glucose uptake and metabolism can be assessed spatially by administering a radioactive glucose analog, 2-deoxy-2-(^{18}F)fluoro-D-glucose (^{18}FDG), and imaging with positron emission tomography (PET) (*9*). Although ^{18}FDG-PET can detect the altered glucose usage with great sensitivity, the high cost and still limited availability in hospitals of PET-CT (computed tomography) hamper its general clinical application. Moreover, the use of radioactive tracers in combination with the additional ionizing radiation of CT detection is not ideal for repeated measurements. Recently, it has become possible to image sugars with magnetic resonance imaging (MRI), exploiting the interaction between hydroxyl protons and water (*10*, *11*). The dynamic imaging of glucose uptake and utilization, named dynamic glucose-enhanced (DGE) MRI, contains information regarding glucose delivery, tissue transport, and metabolism (*12*–*19*). Tolomeo *et al.* (*7*) used DGE MRI to monitor altered glucose uptake in AD mouse brain with 2-deoxy-D-glucose (2-DG) at 7T. They found a lower 2-DG uptake in one AD mouse model (APP23). To facilitate translation to clinical AD diagnosis, however, it is necessary to implement DGE MRI at a 3T clinical field strength (*20*, *21*) and to use nontoxic sugars. We therefore designed an adjusted on-resonance variable delay multiple pulse (onVDMP) MRI (*22*) approach (see Materials and Methods and fig. S1A) to dynamically detect D-glucose delivery, uptake, and utilization in mouse brain on a 3T MRI animal scanner. By adjusting the length of the saturation module of onVDMP MRI, we were able to simultaneously monitor brain parenchyma and CSF in the APP/PS1 and WT mouse brains for two age groups [6 (6M) and 16 months (16M)]. Studying CSF is of interest because recent findings have shown that abnormality of the glymphatic system, a paravascular route for CSF flow through the brain parenchyma, could be a possible feature of AD (*23*, *24*). A typical glymphatic system, which is shown in Fig. 1, is defined as a brain-wide paravascular pathway for CSF and interstitial fluid (ISF) exchange that facilitates efficient clearance of solutes and waste from the brain. Therefore, in addition to brain parenchyma, we studied the uptake and clearance of D-glucose in

[1]Department of Biomedical Engineering, City University of Hong Kong, Hong Kong, China. [2]Russell H. Morgan Department of Radiology and Radiological Science, The Johns Hopkins University School of Medicine, Baltimore, MD, USA. [3]F.M. Kirby Research Center for Functional Brain Imaging, Kennedy Krieger Research Institute, Baltimore, MD, USA. [4]Department of Electrical and Electronic Engineering, The University of Hong Kong, Hong Kong, China. [5]Department of Health Technology and Informatics, The Hong Kong Polytechnic University, Hong Kong, China. [6]Department of Medical Radiation Physics, Lund University, Lund, Sweden. [7]City University of Hong Kong Shenzhen Research Institute, Shenzhen, China.
*Corresponding author. Email: kanniew.y.c@cityu.edu.hk (K.W.Y.C.); xuj@kennedykrieger.org (J.X.)

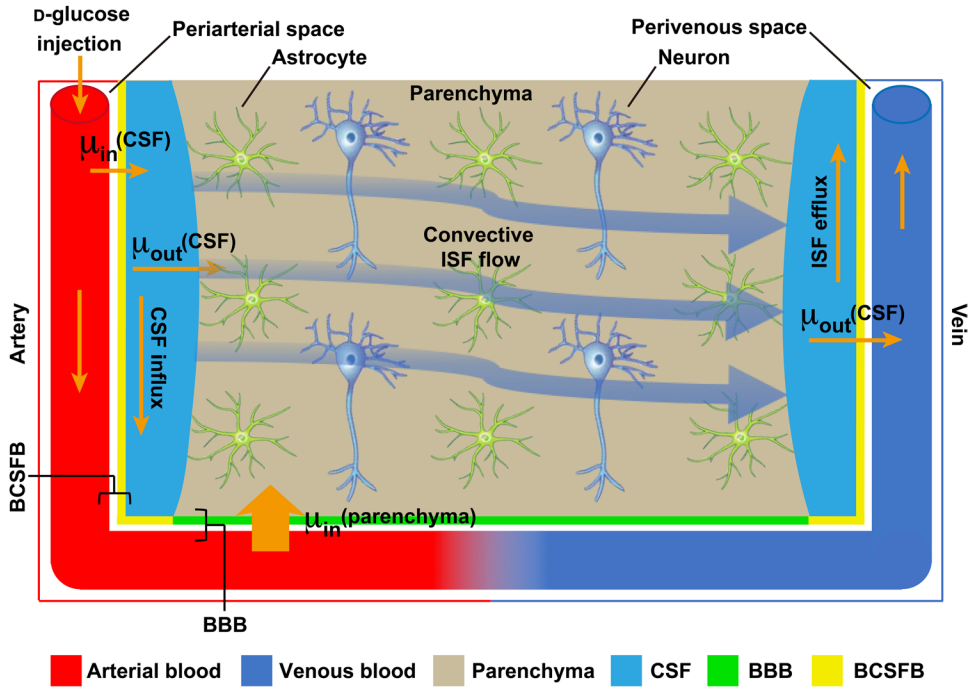

Fig. 1. Schematic diagram of the glucose transportation in the brain. Glucose from the artery enters parenchyma brain and CSF through glucose transporters in the periarterial space, including glucose transporters in blood-CSF barrier (BCSFB) and blood-brain barrier (BBB). A large portion of CSF recirculates to the parenchyma brain and finally drains interstitial fluid (ISF) clearance. μ_{in}, uptake rate; μ_{out}, clearance rate.

CSF as a potential approach to examine the functioning of the glymphatic pathway.

RESULTS

Representative parenchymal and CSF brain images are shown in fig. S2 (A and B). It can be seen from the CSF image that the parenchymal signal is effectively suppressed. For all experiments, blood D-glucose levels were ramped up from about 5 to 30 mM and kept constant (figs. S5 and S6B).

Parenchymal DGE results for WT and APP/PS1 mice

The DGE images of brain parenchyma from young (6M) and old (16M) WT and APP/PS1 mice are shown in Fig. 2 (A to D). The corresponding whole-brain uptake curves show an initial sharp peak of about 1% signal difference for all mice (Fig. 2, E and F). For all four groups of mice, after this initial peak, the parenchymal DGE signal increased gradually until it reached an approximate steady state at about 40 min, which we fitted starting after the minimum following the signal reduction of the initial peak. In young and old APP/PS1 mice, DGE signal in parenchyma was quite stable after this 40-min point. On the contrary, DGE signal decreased in the later stage for parenchyma of 6M and 16M WT mice. While the parenchymal DGE signal levels for younger and older WT mice were comparable, those for older APP/PS1 mice were much lower than in the corresponding young mouse groups (Fig. 2, E and F). In the young groups, the DGE build-up curves of parenchyma showed a high degree of overlap in the first 20 min for both APP/PS1 (6M) and WT (6M) (at 20 min, 1.43 ± 0.49% versus 1.57 ± 0.76%, $P = 0.741$) while a difference became significant after that (at 60 min, 2.15 ± 0.32% versus 1.29 ± 0.43%, $P = 0.007$). In the DGE kinetic curve comparison for the old groups, the DGE signal of APP/PS1 was lower than that of age-matched WT (Fig. 2F) (at 60 min, 0.74 ± 0.08% versus 1.21 ± 0.40%, $P = 0.035$).

The parameters extracted from fitting models can help us to quantitatively assess the D-glucose uptake. Figure 2 (G and H) shows the uptake rate (μ_{in}) and maximal signal intensity (S_{max}) extracted by applying the simple exponential model of Eq. 2 in Materials and Methods. For parenchyma, the DGE signal at equilibrium (S_{max}) (Fig. 2G) showed differences between WT and APP/PS1 in both 6M and 16M groups. In the 6M group, APP/PS1 mice had a trend of slightly higher S_{max} than WT mice (2.16 ± 0.38% versus 1.66 ± 0.59%, $P = 0.151$). Comparing S_{max} to DGE signal differences (Table 1), we see a significantly higher ΔS of APP/PS1 at 60 min compared to that of WT, indicative of slower D-glucose clearance in APP/PS1. On the other hand, APP/PS1 mice in the 16M group had significantly smaller ΔS (0.74 ± 0.08% versus 1.21 ± 0.40%, $P = 0.035$) and S_{max} (0.87 ± 0.09% versus 1.62 ± 0.51%, $P = 0.012$). The S_{max} was similar for both young and old WT mouse groups ($P = 0.904$), suggesting that the S_{max} for WT mice is not strongly age dependent. In contrast, S_{max} of D-glucose decreased significantly for the 16M APP/PS1 group relative to the 6M group ($P < 0.001$). At young age, while μ_{in} of APP/PS1 mice was slightly lower than that of WT mice (0.09 ± 0.03 min^{-1} versus 0.14 ± 0.05 min^{-1}), this did not reach statistical significance ($P = 0.104$). Similar to the S_{max}, the uptake rate of WT mice did not show any clear age dependence ($P = 0.729$), but the rate μ_{in} for APP/PS1 mice was strongly age dependent ($P < 0.001$). While the rate μ_{in} of APP/PS1 mice was slightly higher than those of WT mice in the 16M age groups, this was not significant (0.18 ± 0.02 min^{-1} versus 0.15 ± 0.05 min^{-1}, $P = 0.194$).

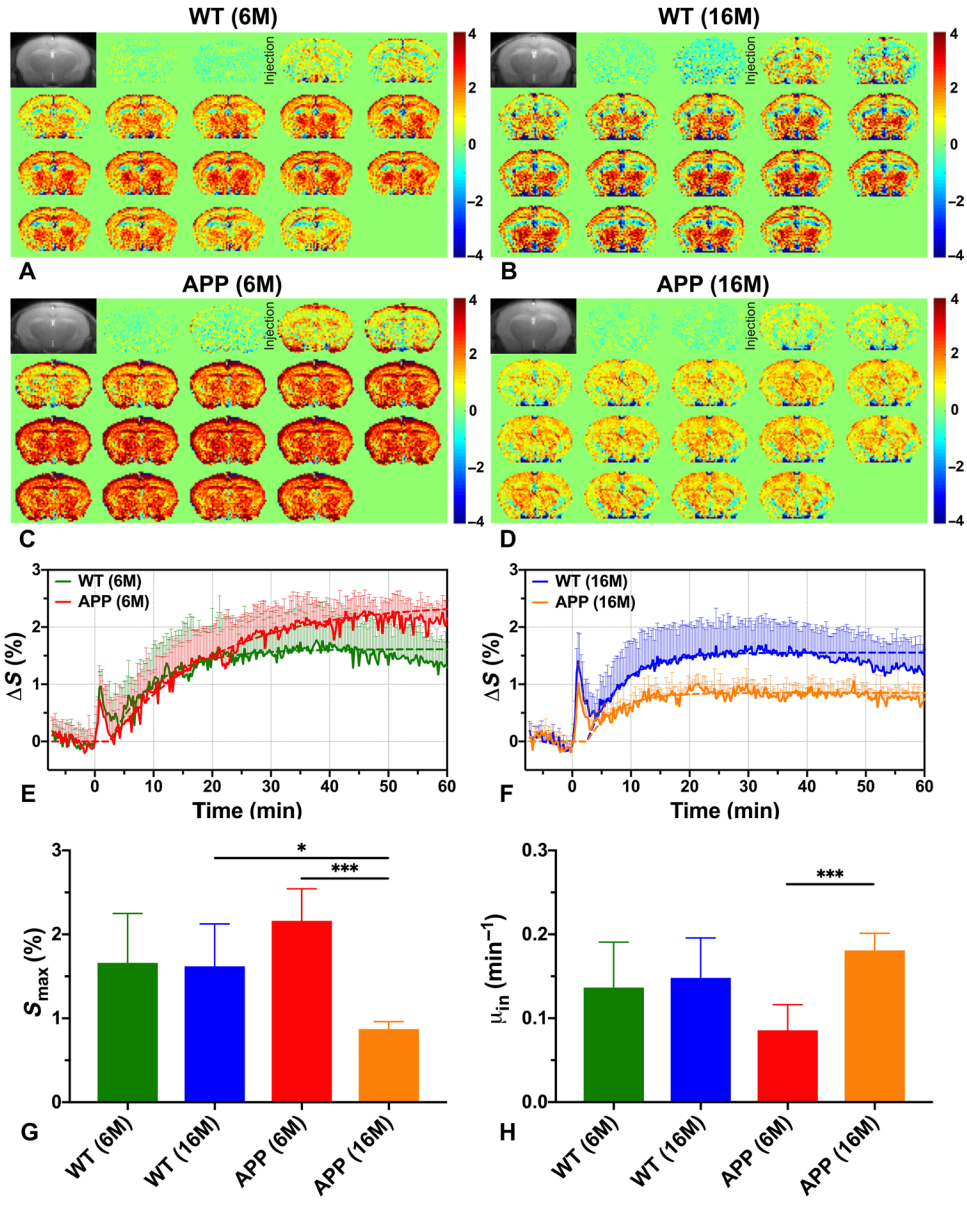

Fig. 2. DGE MRI results for brain parenchyma of WT and APP/PS1 mice. Dynamic difference images before and after D-glucose infusion for WT (**A** and **B**) and APP/PS1 (**C** and **D**) mice at 6M (A and C) and 16M (B and D). DGE images were averaged over sets of 15 for display (18 of 270). Experimental (solid line) and fitted (dashed line) parenchymal DGE curves for WT (6M, $n = 5$) and APP/PS1 (6M, $n = 5$) mice (**E**), as well as WT (16M, $n = 5$) and APP/PS1 (16M, $n = 5$) mice (**F**). Comparison of fitted uptake parameters S_{max} (**G**) and μ_{in} (**H**) between WT and APP/PS1 mice for two age groups (6M and 16M). Significance levels: *$P < 0.05$ and ***$P < 0.001$.

Both S_{max} and μ_{in} suggest that the amount and rate of glucose uptake in the parenchyma of APP/PS1 mice altered substantially with age.

CSF DGE results for WT and APP/PS1 mice

The DGE images for CSF of young (6M) and old groups (16M) are shown in Fig. 3 (A to D). In CSF, the DGE signal rapidly reached a maximum and then gradually washed out, which was quite different from that of parenchyma. In addition to the difference in clearance, the DGE signal intensity was much higher in CSF than parenchyma. The CSF DGE time courses for the WT and APP/PS1 mice are plotted in Fig. 3 (E and F), providing detailed dynamic information about the glucose uptake and clearance. In Fig. 3E, it can be seen that the D-glucose uptake in CSF was initially comparable in the two groups of young mice (ΔS at 2 min, 14.56 ± 2.86% in WT versus 12.70 ± 2.30% in APP/PS1, $P = 0.291$), while the washout phase of WT was obviously faster than that of APP/PS1 (ΔS at 30 min, 3.18 ± 2.95% versus 11.84 ± 4.13%, $P = 0.005$). In the two old groups, the curves of D-glucose in CSF in both WT and APP/PS1 (Fig. 3F) visually resemble the corresponding young groups, except for three features: (i) a somewhat longer plateau for the WT mice, (ii) a reduced initial ΔS for the APP/PS1 mice, and (iii) negligible ΔS

Table 1. Comparison of S_{max} and the parenchymal DGE signal difference at 60 min. ns, not significant.

	S_{max} (%)			ΔS(60 min) (%)			$S_{max} - \Delta S$(60 min) (%)		
	WT	APP	P	WT	APP	P	WT	APP	P
6M	1.66 ± 0.59	2.16 ± 0.38	ns	1.29 ± 0.43	2.15 ± 0.32	**	0.37 ± 0.27	0.01 ± 0.22	*
16M	1.62 ± 0.51	0.87 ± 0.09	*	1.21 ± 0.40	0.74 ± 0.08	*	0.41 ± 0.26	0.13 ± 0.09	*

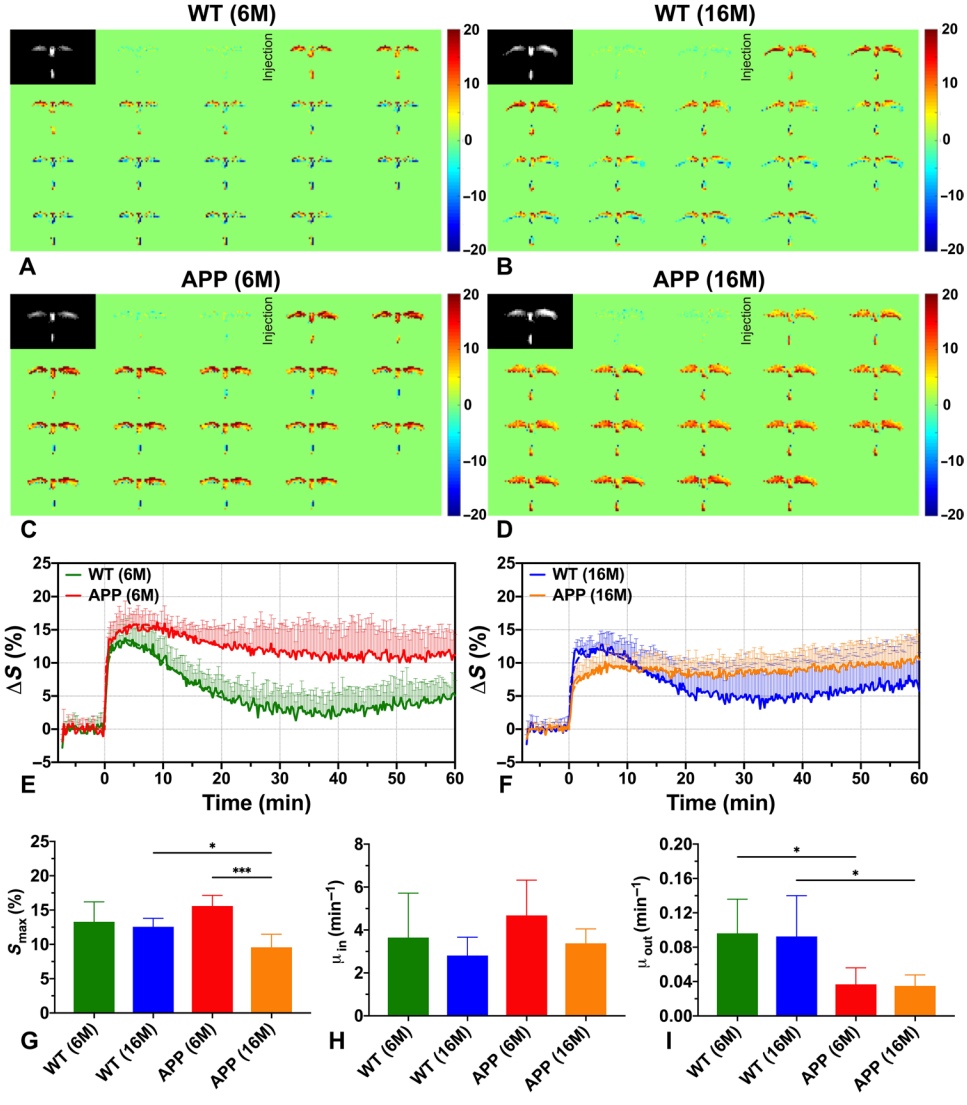

Fig. 3. DGE MRI results for CSF of WT and APP/PS1 mice. Dynamic difference images before and after D-glucose infusion for WT (**A** and **B**) and APP/PS1 (**C** and **D**) mice at 6M (A and C) and 16M (B and D). DGE images were averaged over sets of 15 for display (18 of 270). Experimental (solid line) and fitted (dashed line) CSF DGE curves for WT (6M, $n = 5$) and APP/PS1 (6M, $n = 5$) mice (**E**), as well as WT (16M, $n = 5$) and APP/PS1 (16M, $n = 5$) mice (**F**). Comparison of fitted uptake and clearance parameters S_{max} (**G**), μ_{in} (**H**), and μ_{out} (**I**) between WT and APP/PS1 mice for two age groups (6M and 16M). Significance levels: $^*P < 0.05$ and $^{***}P < 0.001$.

difference between the 5- and 60-min time points for APP/PS1. To estimate quantitative parameters describing the uptake and clearance, we tried to fit several mathematical models. None could accurately fit the whole CSF curve, but using a γ-variate model (see Eq. 3 in Materials and Methods) with three unknowns (S_{max}, μ_{in}, and μ_{out}), we were able to closely fit the uptake and get an initial rate estimate (μ_{out}) for the clearance by fitting only the first 20-min post-infusion. These estimated uptake and clearance parameters are shown in Fig. 3 (G to I). When comparing CSF with parenchyma, the S_{max} values of both WT and APP/PS1 mice were much higher than in brain parenchyma, e.g., 9 to 18% versus 0.8 to 2.6%, respectively, for 6M groups and 7 to 14% versus 0.7 to 2.4%, respectively,

for 16M groups. Despite the higher values, the trend of age dependence for S_{max} was similar for CSF and parenchyma (Figs. 2G and 3G). The S_{max} for APP/PS1 mice was close to that of WT at 6M ($P = 0.156$) but became significantly lower at 16M ($P = 0.019$). Similarly, there was a significant decrease of S_{max} for APP/PS1 mice at 16M compared to 6M ($P < 0.001$), indicating a clear age dependence. There was no substantial difference in D-glucose uptake rate μ_{in} between WT and APP/PS1 mice in either young or old mouse groups (Fig. 3H). The μ_{in} appeared to decrease slightly for both WT or APP/PS1 mice during aging, but this did not reach significance ($P = 0.425$ for WT and $P = 0.141$ for APP/PS1). For the washout initial rates of D-glucose in CSF, μ_{out} was significantly slower in APP/PS1 compared to WT at both 6M ($P = 0.017$) and 16M ($P = 0.031$). This indicates that D-glucose clearance becomes slower in APP/PS1 mice compared to age-matched WT mice. For all mice, the washout was never completed by 60 min, which is in line with the blood glucose level remaining high (fig. S5B).

Regional comparison between APP/PS1 and WT mice

A regional comparison of the parenchymal DGE results for APP/PS1 and WT mice is presented in Fig. 4, using the regions of interest (ROIs) from cortex (CX; yellow frame), hippocampus (HC; purple frame), thalamus (TH; pink frame), and entorhinal cortex (EC; cyan frame) indicated in Fig. 4A. The D-glucose uptake curves in different regions were quite distinctive. For APP/PS1 mice, D-glucose uptake in all four regions at 16M was obviously lower than that at 6M, which is consistent with the overall results in Fig. 2. The DGE curves of CX (Fig. 4B) and TH (Fig. 4D) were quite similar, while the DGE curves of HC (Fig. 4C) and EC (Fig. 4E) showed lower S_{max}. Simple exponential fitting with Eq. 2 showed that no significant changes were found in S_{max} for aging WT mice increase (young, 2.30 ± 0.73% versus old, 2.53 ± 0.79% in CX, $P = 0.653$; young, 1.84 ± 0.63% versus old, 1.97 ± 0.65% in HC, $P = 0.750$; young, 2.49 ± 0.71% versus old, 2.06 ± 0.32%, in TH, $P = 0.253$; young, 1.15 ± 0.36% versus old, 1.25 ± 0.27% in EC, $P = 0.621$). When the APP/PS1 mice get older, alterations were observed uniformly across the brain with a clear decrease of about 1.5% ($P = 0.009$ in CX, $P < 0.001$ in HC, $P < 0.001$ in TH, and $P < 0.001$ in EC) in the S_{max} values (Fig. 4F). For the regional glucose uptake rate μ_{in}, there was no age dependence in WT mice ($P = 0.945$ in CX, $P = 0.775$ in HC, $P = 0.738$ in TH, and $P = 0.396$ in EC), but a clear age dependence was observed in the CX ($P = 0.038$) and TH ($P < 0.001$) regions of AD mice (Fig. 4G). The TH region of young AD mice showed a significant lower μ_{in} compared to age-matched WT mice ($P = 0.028$).

Control experiments

The DGE results of control experiments without any injection ($n = 3$) and with saline injection ($n = 3$) are shown in figs. S3 and S4, respectively. For mice without injection, while these time-dependent images showed some small signal variations at tissue interfaces, during the whole acquisition period in both parenchyma brain and CSF (fig. S3, A and B, respectively), these are negligible compared to with infusion. The dynamic time difference curves of parenchyma and CSF obtained using Eq. 1 in Materials and Methods (fig. S3, C and D, respectively) show signal remaining low over 60 min (0.08 ± 0.38% for parenchyma and 0.39 ± 0.83% for CSF). This indicates excellent scanner stability. Similar results were found in the mice with saline injection (fig. S4), where the dynamic signal differences were −0.15 ± 0.25% and −0.824 ± 1.90% for parenchyma brain and CSF, respectively.

Blood glucose concentration measurements and chemical analysis

A vessel ROI was chosen in the sagittal sinus (yellow box in fig. S5) and corresponding DGE results plotted. We can observe that the D-glucose level in vessels stayed stable after reaching the maximum level. Moreover, the DGE curves of all four mouse groups were consistent, which basically implies that the D-glucose injections are reproducible in these tested mice. Results from blood D-glucose concentration measurements from blood samples taken during infusion outside the magnet are shown in fig. S6A. It can be seen that blood D-glucose reached a level of around 20 to 30 mM that stayed constant within error for at least 60 min, similar to the vessel DGE results. A chemical analysis result showed that some metabolites, especially taurine, serine, and glycine, increased substantially after glucose injection but remained at concentrations of 1 mM or less (fig. S6B).

DISCUSSION

In this study, we demonstrated the feasibility of performing DGE MRI at 3T by using an onVDMP MRI approach that simultaneously measured dynamic D-glucose response curves for both brain parenchyma and CSF. For demonstration of the signal to be due to D-glucose, we performed several validation experiments. Experiments without infusion or saline infusion (figs. S3 and S4) showed negligible dynamic signal changes, indicating a stable setup. We also measured the D-glucose time curve in the sagittal sinus, showing a continuous increase and stabilizing of the signal for all four groups (fig. S5), indicating a low glucose extraction fraction and the D-glucose staying around for a prolonged period of time (at least 60 min at a constant level). We also performed blood glucose concentration measurements (fig. S6A), showing a blood glucose level of 20 to 30 mM for at least 60 min. A low glucose extraction fraction and oxygen extraction fraction are typical for anesthetized mice (*25*). Last, the onVDMP signal, in principle, detects all fast exchanging protons. We therefore also performed chemical analysis of the blood at a time point of 20 min to see whether the slow signal increase could be due to metabolic products of the body (fig. S6B). Several metabolites, especially taurine, serine, and glycine increased substantially but remained at concentrations of 1 mM or less. However, this small concentration, in addition to the level of glucose remaining high in the blood, may explain why the CSF curves increases in intensity at higher time points.

We compared the D-glucose uptake between WT mice and age-matched APP/PS1 transgenic AD mice (6M and 16M), which resemble some of the AD pathology in humans, as well as a reduction of brain glucose uptake (*26*). Notable differences in signal intensity changes and D-glucose uptake were found between the two types of mice for both brain parenchyma and CSF. For parenchyma, to evaluate the rate differences of D-glucose uptake and utilization between AD and WT mice quantitatively, the DGE curve was fitted with an exponential model that provided S_{max}(parenchyma) to represent the maximum glucose uptake level after D-glucose injection for a particular dose and μ_{in}(parenchyma) to reflect the glucose uptake rate. The glucose uptake rate from WT parenchyma ($\mu_{in} = 0.14 \pm 0.05$ min^{-1} for 6M and $\mu_{in} = 0.15 \pm 0.05$ min^{-1} for 16M) measured here with DGE MRI is notably comparable with the D-glucose uptake rate measured by van Zijl *et al.* (*27*) in cat brain using dynamic ^{13}C nuclear magnetic resonance spectroscopy

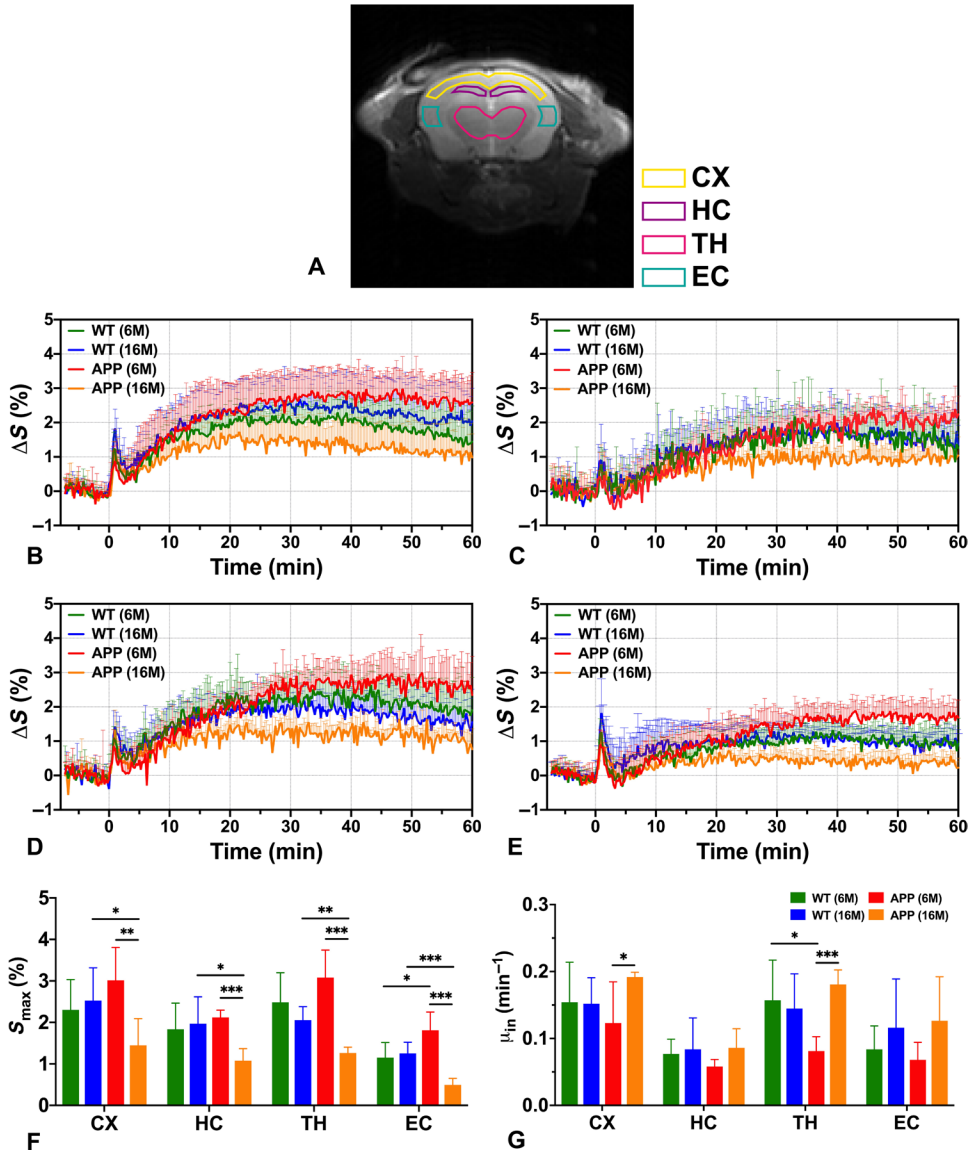

Fig. 4. Regional DGE MRI comparison between WT and AD. (**A**) T2 anatomical image with four regions indicated [yellow, cerebral cortex (CX); purple, hippocampus (HC); pink, thalamus (TH); and cyan, entorhinal cortex (EC)]. DGE curves for both age groups and mouse types are compared for CX (**B**), HC (**C**), TH (**D**), and EC (**E**). Regional S_{max} (**F**) and μ_{in} (**G**) comparison between WT (6M and 16M) and APP/PS1 (6M and 16M). Significance levels: *$P < 0.05$, **$P < 0.01$, and ***$P < 0.001$.

($k_2 + k_3 = 0.136 \pm 0.011$ min^{-1}). This similarity, in addition to the control experiment results, provides strong evidence that the dynamic signal changes detected by here are due predominantly to D-glucose. For the D-glucose uptake in the 6M mouse group, while we did not find significant whole-brain changes for parenchyma ($P = 0.151$, Fig. 2G) in APP/PS1 mice, a regional comparison showed significant differences in EC ($P = 0.032$, Fig. 4F). The first 20 min of parenchymal DGE curves for these four regions are actually very similar for the APP/PS1 (6M) and WT (6M) mice, as can also be seen in the whole-brain results (Fig. 2E). A significant difference in ΔS became apparent in the later 40 min ($P = 0.007$, Fig. 2E and Table 1). A similar increase in glucose uptake in young APP/PS1 mouse has been reported using other imaging modules (*6*, *28*). The histology results in fig. S7 show only limited Aβ plaque in AD mouse brain at this age (*29*). We postulate that the glucose transporter (GLUT) is not very impaired yet at this age in AD mice but that the metabolic rate of glucose has begun to slow down. For the 16M groups, a significantly lower glucose uptake was found in brain parenchyma of APP/PS1 mice compared to the WT mice ($P = 0.012$, Fig. 2G). Moreover, four typical regions studied here (Fig. 4F) also had significantly lower S_{max} values (CX, $P = 0.045$; HC, $P = 0.023$; TH, $P = 0.001$; EC, $P < 0.001$). This could be the result of impaired glucose uptake in AD brain due to the reductions of both GLUT1 and GLUT3 expression at the blood-brain barrier (*30*). Our histology results also show an increased number of plaques in the APP/PS1 mouse brain at age of 16M (fig. S7), which indicates that severe protein aggregation has occurred at this age (*31*).

For CSF, the results in Fig. 3 show that the D-glucose signal (ΔS) is much higher than that in parenchyma and basically reflects the concentration in blood. This can be confirmed from fig. S5B for the

sagittal sinus, which shows a ΔS of about 10%. This slightly lower number for blood compared to CSF is likely due to some partial volume reduction for this small structure and the narrower saturation spectrum for CSF, leading to larger signal differences. From Fig. 3, the DGE CSF curves showed a fast uptake for all groups followed by slow clearance for three groups and negligible clearance for the old APP/PS1 group. We could not find an accurate mathematical model to describe these full curves. However, to obtain a first quantitative estimate of the rate differences of glucose uptake and clearance between AD and WT mice, the DGE CSF curves were fitted for the first 20 min using only a γ-variate model that provided a S_{max}(CSF), an uptake rate μ_{in}(CSF), and an initial rate for clearance, μ_{out}(CSF). The γ-variate model has been applied previously to describe vascular input functions in dynamic contrast-enhanced and dynamic susceptibility-contrast MRI (*32*). In those particular applications for determining perfusion parameters, the kinetics for tracer concentrations of the agent show a fast uptake and clearance. However, the γ-variate function is just a mathematical description for an initial signal rise followed by an exponential decay (Eq. 3 in Materials and Methods). For these mouse DGE MRI experiments, we do not have tracer kinetics due to the initial large volume and the average high concentration of 30 mM in blood (fig. S6), and the signal is not cleared rapidly. However, the γ-variate function was suitable to closely fit the D-glucose uptake in CSF and to obtain an estimate for the initial rate for signal changes following the plateau. If there would be no clearance, then this would give a zero rate, while a continuing increase would give a negative μ_{out}, so this is mathematically straightforward and can describe the possible physiological conditions. For the D-glucose uptake in CSF (S_{max}), we did not find significant changes ($P = 0.156$, Fig. 3G) between WT and APP/PS1 mice for the 6M group, but for the 16M APP/PS1 group, a significantly lower D-glucose uptake was found for APP/PS1 mice compared to the 16M WT mice ($P = 0.019$, Fig. 3G). While the D-glucose uptake rate μ_{in} for CSF did not differ between groups (Fig. 3H), the clearance rate was slower in both young and old APP/PS1 mice (Fig. 3I), compared to WT. The clearance of the D-glucose from CSF could be related to the glymphatic system, which is a paravascular route for CSF flow through the brain parenchyma (*23*). After entering the CSF through the blood-CSF barrier, D-glucose can be recirculated to the parenchyma through the glymphatic pathway (*24*). The substantially reduced CSF clearance rates μ_{out} for 6M and 16M APP mice are consistent with the recent findings that the CSF clearance rate is much smaller in AD mice (*2*, *33*). This reduced CSF clearance detected by DGE could serve as an imaging biomarker to indicate early neuropathology in AD, especially with its distinctive features apart from normal aging as shown in age-matched WT (6M and 16M).

In summary, we demonstrated the capability of onVDMP MRI to detect D-glucose using a 3T MRI scanner, a common clinical field strength. We were able to simultaneously obtain the DGE curves of parenchyma and CSF within one injection. The parenchymal DGE MRI results show a higher D-glucose uptake (ΔS, Table 1) in young AD mice compared to age-matched WT mice, in line with literature (*6*, *28*), while a lower glucose uptake was found in old AD mice, also supported by previously published data (*7*, *34*). We interpreted this in terms of reduced metabolism at young age and reduced transport at old age. Moreover, the washout rate in CSF was substantially lower in young AD mice as compared to age-matched WT mice. Thus, by simultaneously imaging D-glucose kinetics in both parenchyma and CSF, we can reveal glucose uptake, metabolism, and clearance in the brain. We applied a simple fitting in this study to enable us to extract some key parameters for the uptake and clearance trend of DGE curves. A comprehensive model is desired to more fully describe the early neuropathology related to glucose uptake and clearance in the brain. Our results suggest that use of D-glucose as a natural biodegradable contrast agent for MRI has the potential to be a noninvasive method to reveal altered glucose uptake and utilization in both early and late stages of AD, together with altered functioning of glymphatic system for D-glucose clearance.

MATERIALS AND METHODS

Animal preparation

All animal experiments were approved by the Animal Ethics Committee and followed the institutional guidelines of Institutional Laboratory Animal Research Unit of City University of Hong Kong. Animals were housed under standard laboratory conditions, with access to food and water. Ten AD mice (APP/PS1, 5 with an age of 6 months and 5 with an age of 16 months, male, the Jackson laboratory, Maine) and 10 age-matched WT mice (C57BL/6, male, the Jackson laboratory, Maine) were used to study the cerebral glucose uptake and clearance in AD. APP/PS1 mice are double transgenic mice expressing a chimeric mouse/human APP (Mo/HuAPP695swe) and a mutant human PS1 (PS1-dE9), both directed to neurons of the central nervous system. Both mutations are associated with early-onset AD. Another six 6M WT mice were used for the control experiments.

MRI experiments

The onVDMP sequence diagram is shown in fig. S1A. The basic composition of the saturation module is a train of high-power binomial pulses (bp) with zero-bp interval and zero water resonance offset (*22*, *35*, *36*). The pulse shape was two bp, and the number of pulse pairs was four. The peak power strength was 3.1 μT. We used a phase-cycling scheme for onVDMP to improve the resistance to B_0 and B_1 inhomogeneities (*37*). The phase-cycling scheme is $R\overline{R}\overline{R}R$, where R and $\overline{R}$ refer to the phase and alternate phase (+180°), respectively. With this cycling, the acquired signal is robust in minimizing the frequency shift that may be induced by glucose injection (*21*, *38*). The excitation profile in fig. S2C, measured with an onVDMP sequence (60-ms saturation) on WT mouse brain (6M), shows that the signal is stable over a range of about ±50 Hz. Frequency drift due to instability of the scanner (e.g., from heating of the radiofrequency and gradients coils) or due to respiration or glucose injection are typically on the order of 10 Hz and are thus expected to have minimal impact on the onVDMP signal. By setting a different bp number N, we can adjust the saturation length to image the parenchyma and CSF, respectively. In this study, the saturation length was set to 60 ms for imaging parenchyma and 900 ms for imaging CSF. DGE experiments on both parenchyma and CSF images can be acquired in interleaved during one acquisition, as shown in fig. S1B. With the long saturation module, the parenchymal signal can be effectively saturated, as well as enhance the sensitivity of CSF detection. There are several reasons that favor the detection of glucose in CSF at 3T compared to other field strengths. First, the T_2 of CSF at 3T is on the order of 1.6 s and the Z-spectrum narrow, which allows us to more sensitively detect variations. Second, the scaling effect from semisolid magnetization transfer contrast will be minimized since there are no solid-like tissue components.

When carrying out the MRI experiments on mice, anesthesia was induced and maintained using isoflurane at 2 and 1.5%, respectively. The isoflurane was mixed with 90% oxygen generated by an oxygen concentrator. The flow rate of oxygen generator was set to 2 liters/min and kept unchanged during the whole experiment. Mice were placed in a horizontal bore 3T Bruker BioSpec animal scanner (Bruker, Germany). A 82-mm-diameter quadrature coil and a 23-mm-diameter mouse brain surface coil were used for transmitting and receiving signal, respectively. A catheter was placed in the tail vein for glucose administration before placing the animal in the scanner. A bolus of 0.15-ml filtered 50% D-glucose was injected into the mouse body through the tail vein over 1 min (speed, 0.15 ml/min) using an MRI-compatible syringe pump (Harvard Apparatus). Mouse body temperature was maintained at 37°C using a warming pad. Respiration and body temperature were continuously monitored using an MRI-compatible monitor system (SA Instruments Inc.). Before DGE acquisition, the B_0 field over the mouse brain was shimmed using field mapping and second-order shimming. The readout module was rapid acquisition with refocused echoes (RARE) with repetition time (TR)/echo time (TE) = 2.5 s/4.7 ms, RARE factor = 32, centric encoding, slice thickness = 2 mm, and a matrix size of 96 × 96 within a field of view (FOV) of 20 × 20 mm^2, resulting in a time resolution of 15 s for each pair of images (7.5 s for parenchyma and 7.5 s for CSF). A total number of 550 images were acquired for each DGE module, thus leading to a total scanning time of 1 hour 8 min 45 s. The first 10 images were discarded during processing. The glucose injection was started at 8 min 45 s and lasted for 1 min. Hence, the baseline is 7 min 30 s (30 parenchymal images and 30 CSF images), and the monitoring time after glucose injection is 1 hour (240 parenchymal images and 240 CSF images), as shown in Fig. 1B. The image slice was positioned on the basis of a collected sagittal image of the mouse brain with the position of the coronal image slice set to −1.4 mm with respect to the anterior commissure. For the control experiments carried on six 6M WT mice, the MRI protocols and parameters are totally the same, with the details mentioned above, while the injection part is different. Three of them were scanned without any injection to study the stability of the scanner, while the other three mice were injected with saline with same volume, speed, and injection time compared to that of glucose experiments.

Histology experiments

APP/PS1 and C57BL/6 mice were anesthetized with isoflurane and intracardially perfused with phosphate-buffered saline. Whole brains were extracted, fixed for 48 hours in 10% neutral-buffered formalin, and dehydrated in 30% sucrose solution for 72 hours. Coronal slices at 40-μm thickness were cryosectioned and mounted onto charged slides. All amyloid plaques in the brain sections were labeled with antibodies against Aβ (6E10 at 1:500, BioLegend), and the nuclei were visualized by 4′,6-diamidino-2-phenylindole (1 mg/ml) with immunohistochemistry protocol as reported earlier (*39*). The coronal brain sections were imaged with Nikon Eclipse Ti2-E Fluorescence Imaging System at University Research Facility for Life Sciences at The Hong Kong Polytechnic University.

Data analysis

All image processing and data analyses were performed using custom-written code in MATLAB (R2018b, MathWorks, USA). When calculating DGE kinetic curves, baseline signal S_{base} was generated by averaging the 30 baseline images. Since the total number of DGE images was large (270 for each mouse), we averaged every set of 15 images to visualize the dynamic process of glucose changes. Then, we used Eq. 1 for each time point to construct the DGE kinetic curves after glucose administration

$$\Delta S(t) = \frac{S_{base} - S(t)}{S_{base}} \quad (1)$$

The parenchymal and CSF data were processed separately. For the time monitored, after an initial input blip, the DGE uptake curves in parenchyma showed an exponential increase that leveled off around 40 min. We therefore applied an exponential model to fit the DGE uptake after glucose injection

$$\Delta S'_{par}(t) = S_{max}(40\text{min}) \cdot (1 - e^{-\mu_{in}(t-t_0)}) \quad (2)$$

where t_0 indicates the time point of glucose injection, μ_{in} is the glucose uptake rate, and S_{max} is the max DGE signal reached. The DGE data of CSF were different from the DGE curves of parenchyma in showing uptake and clearance over the period measured. We tested several models but could not completely describe the curves. Therefore, we applied a simple γ-variate model (*32*) to fit the DGE data of CSF for only the first 20 min after glucose injection, giving an accurate uptake rate and an estimate of the initial rate of clearance

$$\Delta S'_{CSF}(t) = A \cdot (t - t_0)^{\frac{1}{\mu_{in}}} \cdot e^{-\mu_{out}(t-t_0)} \quad (3)$$

where A is an amplitude modulation parameter, μ_{in} represents the glucose uptake rate, and μ_{out} represents the initial rate of clearance. The maximum signal that CSF DGE reached can be directly extracted after fitting as $S_{max} = \max(\Delta S'_{CSF}(t))$. A schematic diagram about the μ_{in} and μ_{out} for parenchyma and CSF is shown in Fig. 1. For both parenchymal and CSF DGE curves, fitting was achieved using the built-in nonlinear least-squares curve fitting function in MATLAB. When doing the statistical analysis, comparisons were made between groups of mice using the Student's *t* test. Differences were regarded as significant for a P value of <0.05.

SUPPLEMENTARY MATERIALS

Supplementary material for this article is available at http://advances.sciencemag.org/cgi/content/full/6/20/eaba3884/DC1

View/request a protocol for this paper from *Bio-protocol*.

REFERENCES AND NOTES

1. Y. Huang, L. Mucke, Alzheimer mechanisms and therapeutic strategies. *Cell* **148**, 1204–1222 (2012).
2. W. Peng, T. M. Achariyar, B. Li, Y. Liao, H. Mestre, E. Hitomi, S. Regan, T. Kasper, S. Peng, F. Ding, H. Benveniste, M. Nedergaard, R. Deane, Suppression of glymphatic fluid transport in a mouse model of Alzheimer's disease. *Neurobiol. Dis.* **93**, 215–225 (2016).
3. K. Niwa, K. Kazama, S. G. Younkin, G. A. Carlson, C. Iadecola, Alterations in cerebral blood flow and glucose utilization in mice overexpressing the amyloid precursor protein. *Neurobiol. Dis.* **9**, 61–68 (2002).
4. J. Cao, Y. Tang, Y. Li, K. Gao, X. Shi, Z. Li, Behavioral changes and hippocampus glucose metabolism in APP/PS1 transgenic mice via electro-acupuncture at governor vessel acupoints. *Front. Aging Neurosci.* **9**, 5 (2017).
5. F. Luo, N. R. Rustay, U. Ebert, V. P. Hradil, T. B. Cole, D. A. Llano, S. R. Mudd, Y. Zhang, G. B. Fox, M. Day, Characterization of 7- and 19-month-old Tg2576 mice using multimodal in vivo imaging: Limitations as a translatable model of Alzheimer's disease. *Neurobiol. Aging* **33**, 933–944 (2012).
6. G. Poisnel, A.-S. Hérard, N. El Tannir El Tayara, E. Bourrin, A. Volk, F. Kober, B. Delatour, T. Delzescaux, T. Debeir, T. Rooney, J. Benavides, P. Hantraye, M. Dhenain, Increased

regional cerebral glucose uptake in an APP/PS1 model of Alzheimer's disease. *Neurobiol. Aging* **33**, 1995–2005 (2012).
7. D. Tolomeo, E. Micotti, S. C. Serra, M. Chappell, A. Snellman, G. Forloni, Chemical exchange saturation transfer MRI shows low cerebral 2-deoxy-D-glucose uptake in a model of Alzheimer's Disease. *Sci. Rep.* **8**, 9576 (2018).
8. E. Drummond, T. Wisniewski, Alzheimer's disease: Experimental models and reality. *Acta Neuropathol.* **133**, 155–175 (2017).
9. A. Nordberg, J. O. Rinne, A. Kadir, B. Långström, The use of PET in Alzheimer disease. *Nat. Rev. Neurol.* **6**, 78–87 (2010).
10. K. W. Y. Chan, M. T. McMahon, Y. Kato, G. Liu, J. W. M. Bulte, Z. M. Bhujwalla, D. Artemov, P. C. M. van Zijl, Natural D-glucose as a biodegradable MRI contrast agent for detecting cancer. *Magn. Reson. Med.* **68**, 1764–1773 (2012).
11. S. Walker-Samuel, R. Ramasawmy, F. Torrealdea, M. Rega, V. Rajkumar, S. P. Johnson, S. Richardson, M. Gonçalves, H. G. Parkes, E. Årstad, D. L. Thomas, R. B. Pedley, M. F. Lythgoe, X. Golay, *In vivo* imaging of glucose uptake and metabolism in tumors. *Nat. Med.* **19**, 1067–1072 (2013).
12. T. Jin, H. Mehrens, P. Wang, S.-G. Kim, Chemical exchange-sensitive spin-lock MRI of glucose analog 3-O-methyl-d-glucose in normal and ischemic brain. *J. Cereb. Blood Flow Metab.* **38**, 869–880 (2018).
13. D. Kentrup, P. Bovenkamp, A. Busch, K. Schuette-Nuetgen, H. Pawelski, H. Pavenstädt, E. Schlatter, K.-H. Herrmann, J. R. Reichenbach, B. Löffler, B. Heitplatz, V. Van Marck, N. N. Yadav, G. Liu, P. C. M. van Zijl, S. Reuter, V. Hoerr, GlucoCEST magnetic resonance imaging in vivo may be diagnostic of acute renal allograft rejection. *Kidney Int.* **92**, 757–764 (2017).
14. L. Knutsson, A. Seidemo, A. R. Scherman, K. M. Bloch, R. R. Kalyani, M. Andersen, P. C. Sundgren, R. Wirestam, G. Helms, P. C. M. van Zijl, X. Xu, Arterial input functions and tissue response curves in dynamic glucose-enhanced (DGE) Imaging: Comparison between glucoCEST and blood glucose sampling in humans. *Tomography* **4**, 164–171 (2018).
15. F. A. Nasrallah, G. Pagès, P. W. Kuchel, X. Golay, K.-H. Chuang, Imaging brain deoxyglucose uptake and metabolism by glucoCEST MRI. *J. Cereb. Blood Flow Metab.* **33**, 1270–1278 (2013).
16. D. Paech, P. Schuenke, C. Koehler, J. Windschuh, S. Mundiyanapurath, S. Bickelhaupt, D. Bonekamp, P. Bäumer, P. Bachert, M. E. Ladd, M. Bendszus, W. Wick, A. Unterberg, H.-P. Schlemmer, M. Zaiss, A. Radbruch, T1ρ-weighted dynamic glucose-enhanced MR imaging in the human brain. *Radiology* **285**, 914–922 (2017).
17. P. Schuenke, D. Paech, C. Koehler, J. Windschuh, P. Bachert, M. E. Ladd, H.-P. Schlemmer, A. Radbruch, M. Zaiss, Fast and quantitative T1ρ-weighted dynamic glucose enhanced MRI. *Sci. Rep.* **7**, 42093 (2017).
18. A. A. Sehgal, Y. Li, B. Lal, N. N. Yadav, X. Xu, J. Xu, J. Laterra, P. C. M. van Zijl, CEST MRI of 3-O-methyl-D-glucose uptake and accumulation in brain tumors. *Magn. Reson. Med.* **81**, 1993–2000 (2019).
19. X. Xu, K. W. Y. Chan, L. Knutsson, D. Artemov, J. Xu, G. Liu, Y. Kato, B. Lal, J. Laterra, M. T. McMahon, P. C. M. van Zijl, Dynamic glucose enhanced (DGE) MRI for combined imaging of blood–brain barrier break down and increased blood volume in brain cancer. *Magn. Reson. Med.* **74**, 1556–1563 (2015).
20. J. Wang, J. Weygand, K.-P. Hwang, A. S. R. Mohamed, Y. Ding, C. D. Fuller, S. Y. Lai, S. J. Frank, J. Zhou, Magnetic resonance imaging of glucose uptake and metabolism in patients with head and neck cancer. *Sci. Rep.* **6**, 30618 (2016).
21. J. Huang, J. Huang, X. Han, K. W. Y. Chan, J. Xu, C. M. Dong, L. Chen, E. X. Wu, P. Van Zijl, Impaired glucose uptake in mouse brain with Alzheimer's disease detected by dynamic glucose enhanced (DGE) MRI at 3T. *Alzheimers Dement.* **15**, 747 (2019).
22. J. Xu, K. W. Y. Chan, X. Xu, N. Yadav, G. Liu, P. C. M. van Zijl, On-resonance variable delay multipulse scheme for imaging of fast-exchanging protons and semisolid macromolecules. *Magn. Reson. Med.* **77**, 730–739 (2017).
23. S. Da Mesquita, A. Louveau, A. Vaccari, I. Smirnov, R. C. Cornelison, K. M. Kingsmore, C. Contarino, S. Onengut-Gumuscu, E. Farber, D. Raper, K. E. Viar, R. D. Powell, W. Baker, N. Dabhi, R. Bai, R. Cao, S. Hu, S. S. Rich, J. M. Munson, M. B. Lopes, C. C. Overall, S. T. Acton, J. Kipnis, Functional aspects of meningeal lymphatics in ageing and Alzheimer's disease. *Nature* **560**, 185–191 (2018).
24. J. J. Iliff, M. Wang, Y. Liao, B. A. Plogg, W. Peng, G. A. Gundersen, H. Benveniste, G. E. Vates, R. Deane, S. A. Goldman, E. A. Nagelhus, M. Nedergaard, A paravascular pathway facilitates CSF flow through the brain parenchyma and the clearance of interstitial solutes, including amyloid β. *Sci. Transl. Med.* **4**, 147ra111 (2012).
25. A. W. Loepke, J. C. McCann, C. D. Kurth, J. J. McAuliffe, The physiologic effects of isoflurane anesthesia in neonatal mice. *Anesth. Analg.* **102**, 75–80 (2006).
26. L. Mosconi, R. Mistur, R. Switalski, W. H. Tsui, L. Glodzik, Y. Li, E. Pirraglia, S. de Santi, B. Reisberg, T. Wisniewski, M. J. de Leon, FDG-PET changes in brain glucose metabolism from normal cognition to pathologically verified Alzheimer's disease. *Eur. J. Nucl. Med. Mol. Imaging* **36**, 811–822 (2009).
27. P. C. Van Zijl, D. Davis, S. M. Eleff, C. T. Moonen, R. J. Parker, J. M. Strong, Determination of cerebral glucose transport and metabolic kinetics by dynamic MR spectroscopy. *Am. J. Physiol.* **273**, E1216–E1227 (1997).
28. X.-Y. Li, W.-W. Men, H. Zhu, J.-F. Lei, F.-X. Zuo, Z.-J. Wang, Z.-H. Zhu, X.-J. Bao, R.-Z. Wang, Age- and brain region-specific changes of glucose metabolic disorder, learning, and memory dysfunction in early Alzheimer's disease assessed in APP/PS1 transgenic mice using ^{18}F-FDG-PET. *Int. J. Mol. Sci.* **17**, 1707 (2016).
29. T. M. Wengenack, S. Whelan, G. L. Curran, K. E. Duff, J. F. Poduslo, Quantitative histological analysis of amyloid deposition in Alzheimer's double transgenic mouse brain. *Neuroscience* **101**, 939–944 (2000).
30. I. A. Simpson, K. R. Chundu, T. Davies-Hill, W. G. Honer, P. Davies, Decreased concentrations of GLUT1 and GLUT3 glucose transporters in the brains of patients with Alzheimer's disease. *Ann. Neurol.* **35**, 546–551 (1994).
31. M. Garcia-Alloza, E. M. Robbins, S. X. Zhang-Nunes, S. M. Purcell, R. A. Betensky, S. Raju, C. Prada, S. M. Greenberg, B. J. Bacskai, M. P. Frosch, Characterization of amyloid deposition in the APPswe/PS1dE9 mouse model of Alzheimer disease. *Neurobiol. Dis.* **24**, 516–524 (2006).
32. T. Benner, S. Heiland, G. Erb, M. Forsting, K. Sartor, Accuracy of gamma-variate fits to concentration-time curves from dynamic susceptibility-contrast enhanced MRI: Influence of time resolution, maximal signal drop and signal-to-noise. *Magn. Reson. Imaging* **15**, 307–317 (1997).
33. Q. Ma, B. V. Ineichen, M. Detmar, S. T. Proulx, Outflow of cerebrospinal fluid is predominantly through lymphatic vessels and is reduced in aged mice. *Nat. Commun.* **8**, 1434 (2017).
34. M. Sadowski, J. Pankiewicz, H. Scholtzova, Y. Ji, D. Quartermain, C. H. Jensen, K. Duff, R. A. Nixon, R. J. Gruen, T. Wisniewski, Amyloid-β deposition is associated with decreased hippocampal glucose metabolism and spatial memory impairment in APP/PS1 mice. *J. Neuropathol. Exp. Neurol.* **63**, 418–428 (2004).
35. D. Wu, J. Xu, J. Lei, M. Mclane, P. C. van Zijl, I. Burd, Dynamic glucose enhanced MRI of the placenta in a mouse model of intrauterine inflammation. *Placenta* **69**, 86–91 (2018).
36. X. Xu, J. Xu, K. W. Y. Chan, J. Liu, H. Liu, Y. Li, L. Chen, G. Liu, P. C. M. van Zijl, GlucoCEST imaging with on-resonance variable delay multiple pulse (onVDMP) MRI. *Magn. Reson. Med.* **81**, 47–56 (2019).
37. M. H. Levitt, *Spin Dynamics: Basics of Nuclear Magnetic Resonance* (John Wiley & Sons, 2001).
38. M. Zaiss, K. Herz, A. Deshmane, M. Kim, X. Golay, T. Lindig, B. Bender, U. Ernemann, K. Scheffler, Possible artifacts in dynamic CEST MRI due to motion and field alterations. *J. Magn. Reson.* **298**, 16–22 (2019).
39. K.-H. Tse, K. Herrup, Re-imagining Alzheimer's disease–the diminishing importance of amyloid and a glimpse of what lies ahead. *J. Neurochem.* **143**, 432–444 (2017).

Acknowledgments

Funding: We are grateful to receive funding support from the Research Grants Council (9042620), City University of Hong Kong (9610362, 7005210, and 6000660), National Institutes of Health (R01EB019934), Swedish Research Council 2015-04170 and 2019-03637, and Swedish Cancer Society CAN2015/251 and CAN2018/550. **Author contributions:** J.H. performed all the MRI experiments, analyzed and interpreted the data, and drafted the manuscript. P.C.M.v.Z. directed the data analysis and interpretation. X.H., J.H.C.L., and K.W.Y.C. were involved in MRI experiments. X.H., G.W.Y.C., and K.-H.T. performed the immunohistology experiments. C.M.D. and E.X.W. prepared the AD mouse models. L.K. contributed to the data interpretation. L.C. contributed to the data analysis. J.X. and K.W.Y.C. directed the project and experimental design, contributed to data analysis and interpretation, and drafted the manuscript. All authors edited the manuscript. **Competing interests:** The authors declare that they have no competing interests. **Data and materials availability:** All data needed to evaluate the conclusions in the paper are present in the paper and/or the Supplementary Materials. Additional data related to this paper may be requested from the authors.

Submitted 29 November 2019
Accepted 27 February 2020
Published 13 May 2020
10.1126/sciadv.aba3884

Citation: J. Huang, P. C. M. van Zijl, X. Han, C. M. Dong, G. W. Y. Cheng, K.-H. Tse, L. Knutsson, L. Chen, J. H. C. Lai, E. X. Wu, J. Xu, K. W. Y. Chan, Altered D-glucose in brain parenchyma and cerebrospinal fluid of early Alzheimer's disease detected by dynamic glucose-enhanced MRI. *Sci. Adv.* **6**, eaba3884 (2020).

Science Advances

Altered d-glucose in brain parenchyma and cerebrospinal fluid of early Alzheimer's disease detected by dynamic glucose-enhanced MRI

Jianpan Huang, Peter C. M. van Zijl, Xiongqi Han, Celia M. Dong, Gerald W. Y. Cheng, Kai-Hei Tse, Linda Knutsson, Lin Chen, Joseph H. C. Lai, Ed X. Wu, Jiadi Xu and Kannie W. Y. Chan

Sci Adv **6** (20), eaba3884.
DOI: 10.1126/sciadv.aba3884